**ADVANCED
ENERGY
MATERIALS**

Supporting Information

Textile-Type Lithium-Ion Battery Cathode Enabling High Specific/Areal Capacities and High Rate Capability through Ligand Replacement Reaction-Mediated Assembly

Minseong Kwon, Donghyeon Nam, Seokmin Lee, Yongju Kim, Bongjun Yeom, Jun Hyuk Moon, Seung Woo Lee,* Yongmin Ko,* and Jinhan Cho*

Supporting Information

Textile-Type Lithium-Ion Battery Cathode Enabling High Specific/Areal Capacities and High Rate Capability through Ligand Replacement Reaction-Mediated Assembly

Minseong Kwon, Donghyeon Nam, Seokmin Lee, Yongju Kim, Bongjun Yeom, Jun Hyuk Moon, Seung Woo Lee[*], Yongmin Ko[*], and Jinhan Cho[*]

Experimental Section

Materials: Cellulose textile was purchased from NamYang Nonwoven Fabric Co. Ltd. (Republic of Korea), and multiwalled carbon nanotubes (MWNTs, diameter 7~9 nm, length 10~50 μm, purity >80 %) was purchased from Nanosolution Co. Ltd. (Republic of Korea). Oleic acid (>98% purity) was purchased from Uniam Co. Ltd. (Republic of Korea). 1-(3-Dimethylaminopropyl)-3-ethylcarbodiimide methiodide (i.e., EDC, 98 % purity) was purchased from Alfa Aesar. The other chemical reagents were purchased from Sigma−Aldrich and used without further purification.

Synthesis of DA-LFP NPs: First, dioleamide (i.e., DA), as a stabilizer, was prepared by condensation reaction of an oleic acid (90 mmol)/oleylamine (90 mmol) mixture (molar ratio:

1:1) at 70 °C for 1 h in a vacuum condition. In this case, considering that the molar ratio of OA and OAm in DA has a significant effect on the physical properties of resulting nanocrystals such as crystal size, morphology, shape, and crystallinity, the ratio of OA and OAm was adjusted to 1:1 while carefully controlling other synthesis conditions (i.e., reaction time, heating rate, and target temperature). After 1 h, iron (II) diacetate (4 mmol) and lithium acetate (4 mmol) were added to the mixture, and the mixture was continuously stirred for an additional 30 min under the same reaction conduction until the color of the solution turned black. Sequentially, phosphoric acid (4 mmol) was injected into the above-mentioned mixture and kept in a vacuum condition to remove residual moisture. When the color of the solution turned to transparent green, the reaction temperature was rapidly increased to 350 °C under an argon atmosphere and maintained for 2 h (solution color changed to white yellow). After cooling down the mixture to the room temperature, the unreacted organic residuals were washed out using the mixture of ethanol/acetone as a poor solvent by centrifugation. The as-synthesized DA-LFP NPs were dispersed in toluene for use in experiments.

Chemical modification of MWNTs: Carboxylic acid-functionalized MWNT (MWNT-COOH) was first prepared by strong acid treatment with H_2SO_4/HNO_3 at 70 °C for 3 h. After the reaction, the resulting MWNT-COOH was purified through centrifugation and vacuum filtration to remove residual acid. As-prepared MWNT-COOH was re-dispersed in ethanol. The amine-functionalized MWNT (i.e., MWNT-NH_2) was prepared through ester coupling reaction based on the MWNT-COOH. Briefly, the suspension of MWNT-COOH (80 mL, 0.5 mg mL^{-1} in ethanol) were reacted with excess of ethylenediamine (>99 % purity, Sigma-Aldrich) under vigorous stirring for 5 h in the presence of 800 mg 1-(3-Dimethylamino propyl)-3-ethylcarbodiimide methiodide (EDC, 98 % purity, Alfa Aesar). The resulting

suspension was dialyzed (MWCO 12000-14000) to remove byproducts and residuals. The resulting MWNT-NH$_2$ was also re-dispersed in ethanol for LbL assembly.

Conductive textiles for current collector: A piece of cleaned cellulose textile was first immersed into polyethyleneimine (PEI, 5 mg mL^{-1} dispersed in ethanol) solution for 30 min to introduce amine groups to the surface. Then, the fully dried PEI-coated textile substrates were immersed into the MWNT-COOH solution for 20 min. After washing and drying the textile substrate (i.e., MWNT-COOH-coated textile), the MWNT-NH$_2$ was coated by dipping the textile into the MWNT-NH$_2$ solution for 20 min. These processes were repeated until the desired bilayer number was obtained that would impart adequate electrical conductivity to the textile at a current collector.

(DA-LFP NP/MWNT-composite)$_m$-coated textile electrodes: Textile-based cathode electrode was prepared though ligand-exchange reaction (LRR)-induced LbL assembly of DA-LFP NP and functionalized MWNTs (i.e., MWNT-COOH and MWNT-NH$_2$) onto the as-prepared conductive textile substrates (i.e., MWNT multilayer-coated textile) in organic media. First, the conductive textile substrates were dipped into the DA-LFP NP solution (10 mg mL^{-1} in toluene) for 20 min. After rinsing with pure toluene and drying completely, the textiles were immersed in the MWNT-NH$_2$ solution (2 mg mL^{-1} in ethanol) for 20 min. In this process, the bulky organic ligands (i.e., DA) bound to the LFP NP are replaced with NH$_2$ groups of MWNT-NH$_2$. Then, the textiles with the MWNT-NH$_2$ outermost layer were sequentially dipped into MWNT-COOH and MWNT-NH$_2$ solution for 20 min, respectively, to form MWNT-NH$_2$/MWNT-COOH/MWNT-NH$_2$ multilayers. In this study, the formed MWNT-NH$_2$/MWNT-COOH/MWNT-NH$_2$ multilayers is abbreviated as MWNT-composite. This LRR assembly between DA-LFP NP and MWNT-composite was repeated until desired periodic number (m).

Conventional slurry-cast textile electrodes: Active slurry was prepared by the mechanical blending of LFP powder (average diameter of ~5 μm, Sigma Aldrich), surface functionalized MWNTs (MWNT-COOH and MWNT-NH$_2$), and polyvinylidene fluoride (PVDF, MTI Korea) with weigh ratio of 6.5:2.5:1. 1-Methyl-2-pyrrolidinone (NMP, Sigma Aldrich) was used as a solvent. The formed slurry was applied to the conductive textile (i.e., MWNT multilayer-coated cellulose textile) by doctor-blading technique, and then completely dried at 70 °C in a vacuum oven for 3 h to fabricate a battery cell.

Characterization: High-resolution Transmission electron microscopy (HR-TEM) was conducted using a Technai 20 instrument (FEI). Field-emission scanning electron microscopy (FE-SEM) and energy-dispersive X-ray spectroscopy (EDS) mapping images were obtained using an S-4800 instrument (Hitachi). Surface chemistry and build-up mechanism of LRR-assembled electrodes were conducted by Fourier transform infrared (FTIR) analysis using a CARY 600 spectrometer (Agilent Technologies) in a specular mode with a resolution of 4 cm^{-1} at room temperature in atmosphere and the obtained data were plotted with spectral analysis software (OMNIC, Nicolet). All spectra were obtained from 200 scans. UV-vis spectra of the LRR-assembled multilayers were obtained from a Lambda 35 instrument (Perkin Elmer). X-ray diffraction (XRD) analysis was performed using SmartLab (Rigaku). X-ray photoelectron spectroscopy (XPS) analysis was conducted using X-TOOL (ULVAC-PHI). The collected all XPS spectra were calibrated based on the C 1s peak at 284.5 eV. The quantitative growth behavior of LRR-assembled multilayer films was monitored using a quartz crystal microgravimetry (QCM 200, SRS).

Electrochemical measurements: Electrochemical tests, including cyclic voltammetry (CV), galvanostatic charge/discharge (GCD) measurement, and electrochemical impedance spectroscopy (EIS), were carried out using WBCS3000 multichannel workstation and MP2A

(Wan A Tech., Republic of Korea). All electrodes for the testing were prepared in a coin-type half-cell (CR2032, MTI Korea) using a piece of lithium foil as counter and reference electrodes, which were performed in an argon-filled glovebox (MBraun, $O_2 < 0.1$ ppm, H_2O < 0.1 ppm). A mixture of ethylene carbonate and dimethyl carbonate with a volume ratio of 3:7 (EC/DMC, Panax Etec Co., Ltd.) dissolved 1 M $LiPF_6$ was used as an electrolyte. The specific and areal capacities of the textile cathode electrodes measured with a potential window of 1.8 – 4.2 V at various sweep rates. In this case, the all capacity values (i.e., specific and areal capacities) were calculated from the total weight of active materials including LFP NP and MWNTs. EIS measurements were carried out at open circuit voltage (OCV, ~3.0 V for each electrode) in frequency range of 100 kHz – 0.01 Hz with a perturbation amplitude of 0.01 mV. The collected impedance dataset was analyzed by fitting in Randle's equivalent circuits using ZMAN software (Wan A Tech.). The diffusion coefficient (*D*) of the textile electrodes was calculated from Warburg impedance coefficient (σ_w) by the following equation:

$$Z' = R_s + R_{ct} + \sigma_w \square^{-0.5} \qquad\qquad (1)$$

$$D = 0.5 \, (RT/AF^2\sigma_w C)^2 \qquad\qquad (2)$$

where, $\square$, *R*, *T*, *A*, *F*, and *C* indicate angular frequency, gas constant, absolute temperature, electrode area, Faraday's constant, and molecular concentration of electrolyte ions, respectively.

Electrochemical impedance spectra: The Nyquist plots of each textile electrode prepared by LbL assembly and slurry casting methods showed a typical impedance spectrum feature consisting of a semicircular arc intercept on real-axis (resistance, *Z'*) in the high-to-middle frequency region and a Warburg line sloping along the imaginary-axis (reactance, –*Z''*) in the low-frequency region, which can be simplified to an equivalent circuit model for a half-cell

system with a constant phase element (CPE) for more accurate fitting (inset of **Figure 3e**). In present study, since the electrode composition and the amount (ratio) of the conductive enhancer (i.e., MWNTs) capable of forming an electron pathway to the current collector (i.e., conductive textile substrate) are about the same, the R_s values were measured as similar values of ~4.7 and ~4.8 Ω cm^{-2} for the LRR-assembled electrode and the slurry-cast electrode, respectively. However, the efficient interfacial design through LRR assembly significantly lowered the Rct value (39.3 Ω cm^{-2}) compared to the conventional slurry casting method (98.4 Ω cm^{-2}).

Additionally, as confirmed in earlier section, unlike the LbL-assembled electrodes, the slurry casting method can clog the pores of the textiles due to partial agglomerations, creating a number of dead-end pores in the electrode (i.e., active composite layer on textile surface), which also limit fast charge transfer and ion (Li) diffusion/migration to the porous active layer. Accordingly, the diffusion coefficient (D) of each electrode calculated by Warburg impedance (Z_w) was recorded as 5.4×10^{-13} and 1.2×10^{-14} cm^2 s^{-1} for the LbL-assembled electrode and the slurry-cast electrode, respectively, implying superior ion diffusion behavior of the LbL-assembled electrodes enabling high rate capability (**Figure S19**).

We also monitored the change in impedance spectra after GCD cycling (**Figure S20**). For each electrode, the R_{ct} values were reduced after the 50 cycles due to the improved electrolyte wettability enabling easier electrochemical activation of the active materials. On the other hand, another depressed semicircular arc related to the resistance in the cathode-electrolyte-interphase (CEI) layer has newly appeared in the high-frequency region after GCD cycling. In general, the formation of stable and uniform CEI layer on the cathode surface (i.e., at electrode/electrolyte interface) during charge/discharge processes has a great

influence on battery performance, such as long-term cycle stability with high Coulombic efficiency, which is more pronounced in the lithium metal anode-based battery cells. Additionally, it has also been reported that the formation of the CEI layer is highly sensitive to the uniform surface distribution of the cathode material, as well as to operating conditions such as cut-off voltage, electrolyte composition, and/or applied current. In this regard, the much lower R_{CEI} value of the LbL-assembled electrode (~0.07 Ω cm^{-2}) than the slurry-cast electrode (~7 Ω cm^{-2}) may imply that the uniformly coated LFP NPs on the MWNT networks significantly reduce the indiscriminate electrolyte decomposition at electrode/electrolyte interfaces, allowing for a stable CEI layer and better performance retention.
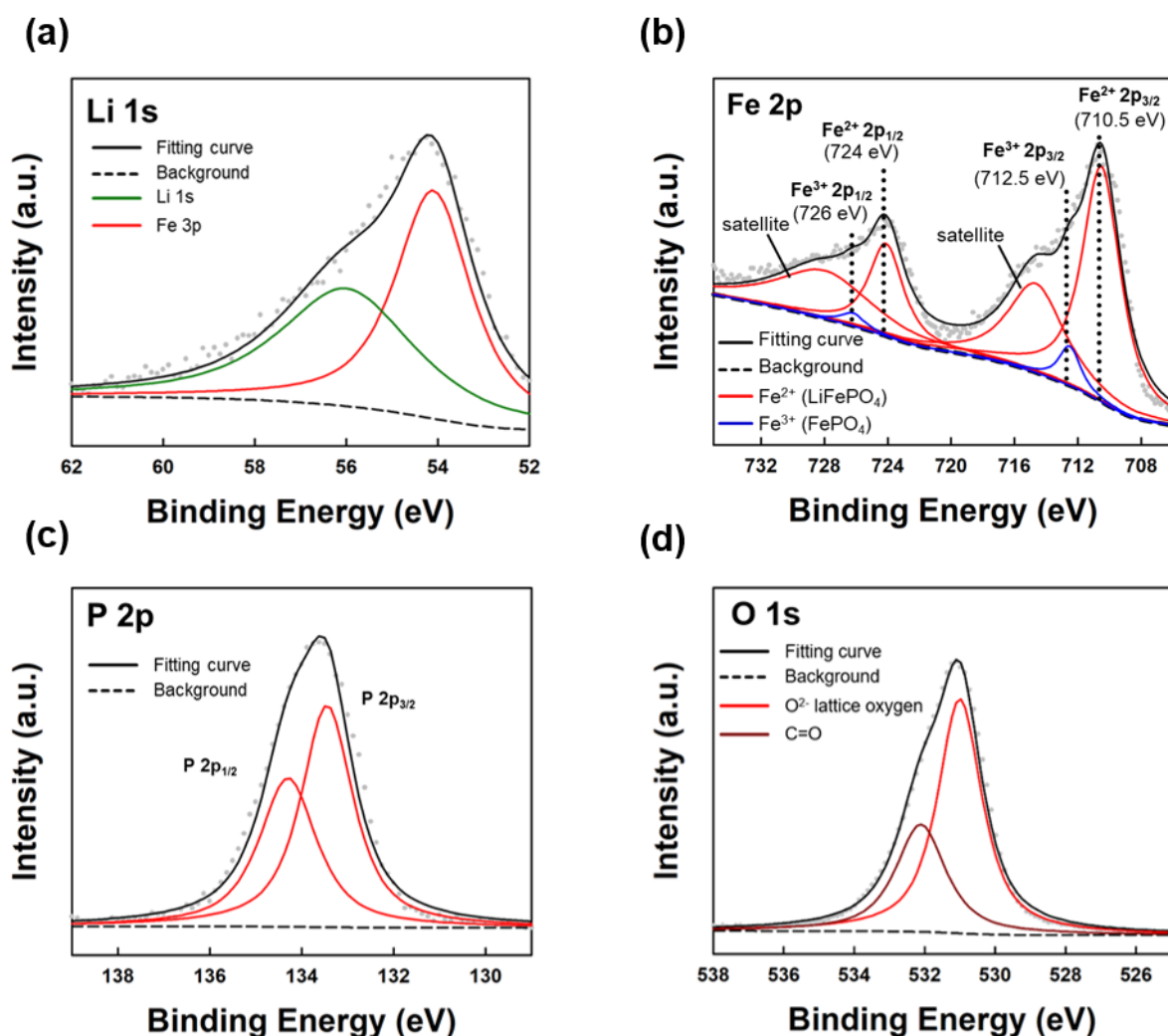
Figure S1. XPS spectra of (a) Li 1s, (b) Fe 2p, (c) P 2p, and (d) O 1s for the DA-LiFePO$_4$ NPs. The Fe 2p doublet spectra caused by spin-orbit coupling were observed at 710.5 (Fe 2p$_{1/2}$) and 724 eV (Fe 2p$_{3/2}$) with corresponding satellite peaks (at 714 and 727.8 eV) originating from typical characteristics of transition metal ions containing partially filled *d*-orbits.[S1–S3] In this case, these two core spectra for Fe 2p with a binding energy separation of ~14 eV reflect the oxidation state of Fe^{2+} in the olivine-type LiFePO$_4$ structure.[S4,S5] Additionally, the only one P 2p doublet (P 2p$_{1/2}$ and P 2p$_{3/2}$) and narrow O 1s spectrum at 133.6 and 531.2 eV are attributed to the phosphate component (PO$_4^{3-}$), further demonstrating the well-synthesized LFP NPs.[S11] Particularly, the Fe 2p spectra have slight traces for Fe^{3+} ions reflecting the presence of FePO$_4$, indicating that the lithium-rich LFP NPs dominate in

the final products.[S2] Therefore, these results clearly demonstrate the successful synthesis of the well-defined single-crystalline DA-LFP NP.
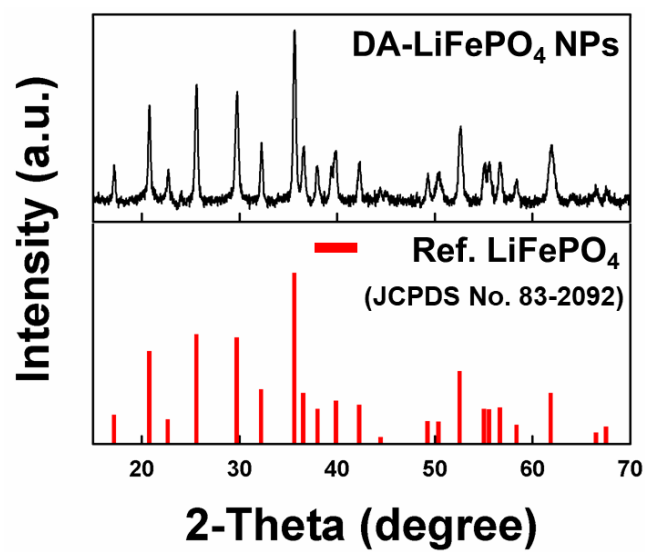
Figure S2 XRD patterns of synthesized DA-LFP NPs (top) with typical LiFePO$_4$ crystals (bottom; JCPDS No. 83-2092).

Figure S3. Digital images of DA-LFP NP solution showing excellent dispersion stability in toluene without any noticeable precipitation even after six months.
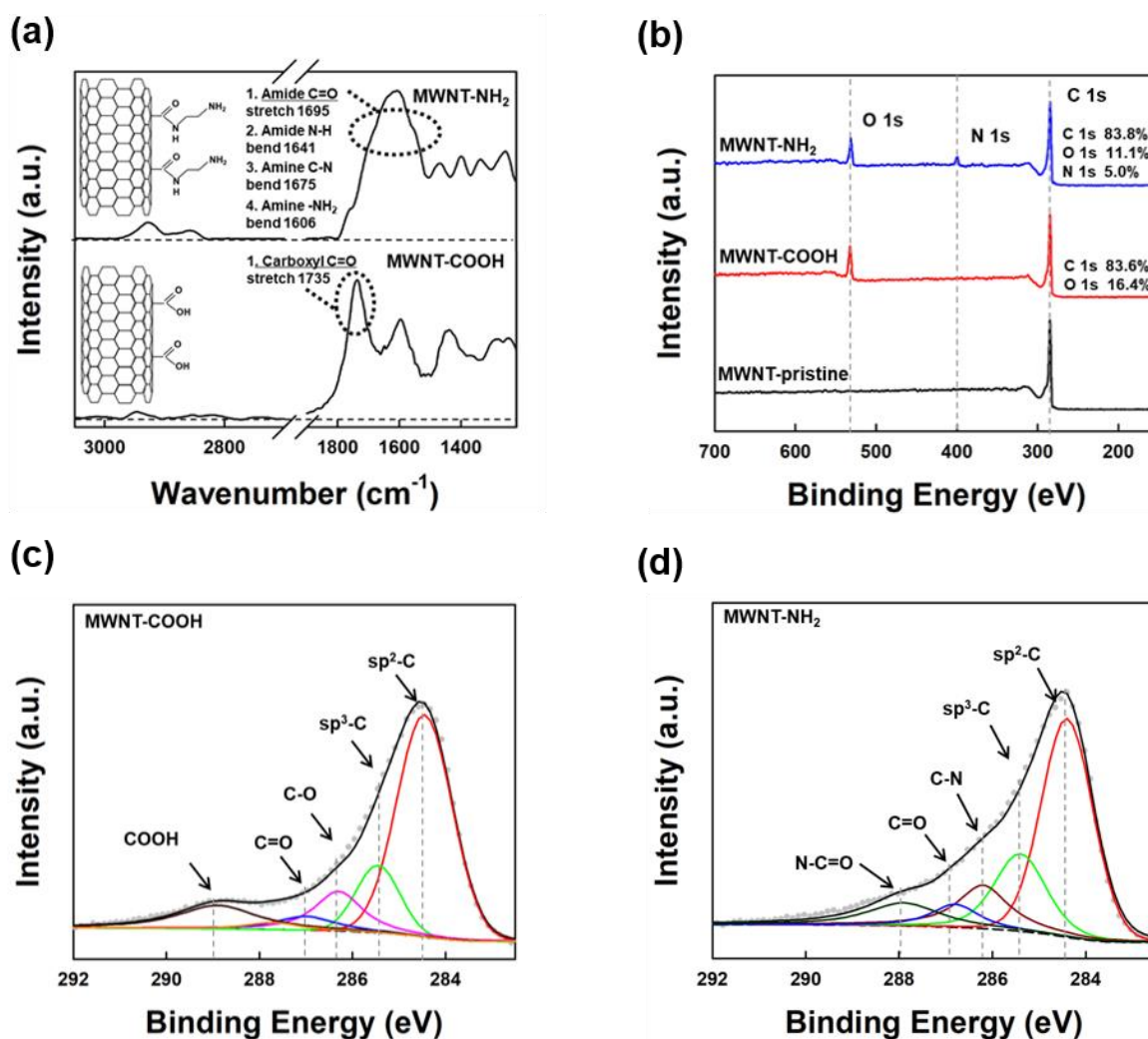
Figure S4. (a) Characteristic FTIR spectra and schematic diagrams of functionalized MWNT-NH$_2$ and MWNT-COOH (inset). In this case, the MWNT-COOH showed a notable peak at 1735 cm^{-1}, corresponding to the C=O group of carboxylic acid, and the new peaks appeared at round 1605 ~ 1695 cm^{-1} originating from amide structure and primary amine groups after amine functionalization (i.e., MWNT-NH$_2$).[S6] (b) Wide scan XPS survey for pristine MWNT, MWNT-COOH, and MWNT-NH$_2$. The MWNT-NH$_2$ showed binding energy peak of N 1s that was not detected in MWNT-COOH and pristine MWNT, which is attributed to amine groups as shown in FTIR analysis. Deconvoluted XPS C 1s spectra for (c) MWNT-COOH and (d) MWNT-NH$_2$. Here, the new binding energies centered at 286.2 and 287.9 eV generated by C-N (from NH$_2$) and N-C=O of formed amide bonds could be seen,

which further suggest successful surface modification *via* amine-terminated molecule-based ester coupling.
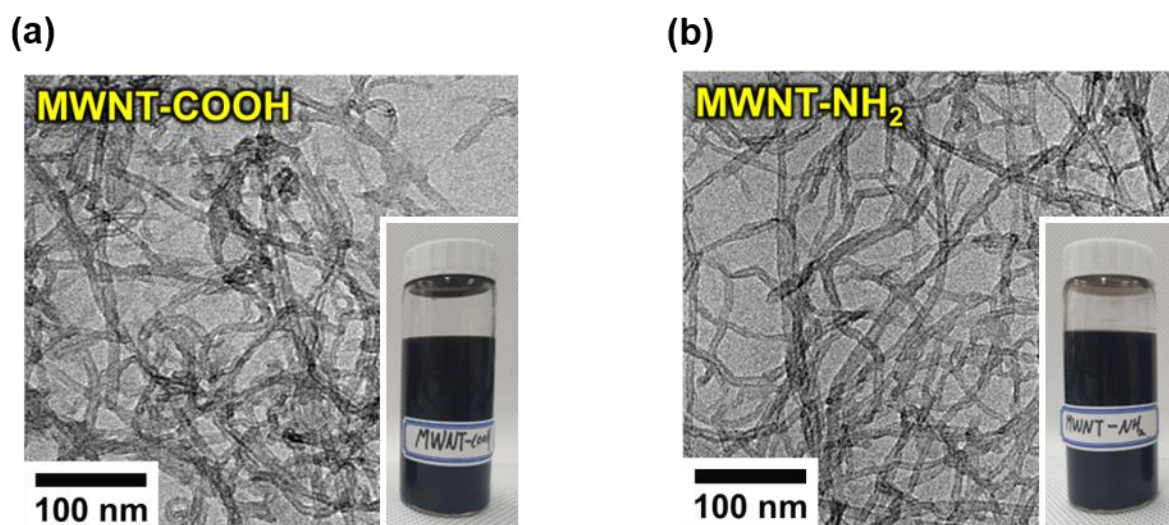
Figure S5. TEM images of the drop-casted (a) MWNT-COOH and (b) MWNT-NH$_2$. In this case, the MWNTs perfectly preserved the intrinsic tubular shape even after sequential surface modification processes. Insets indicate each MWNT solution dispersed in ethanol.
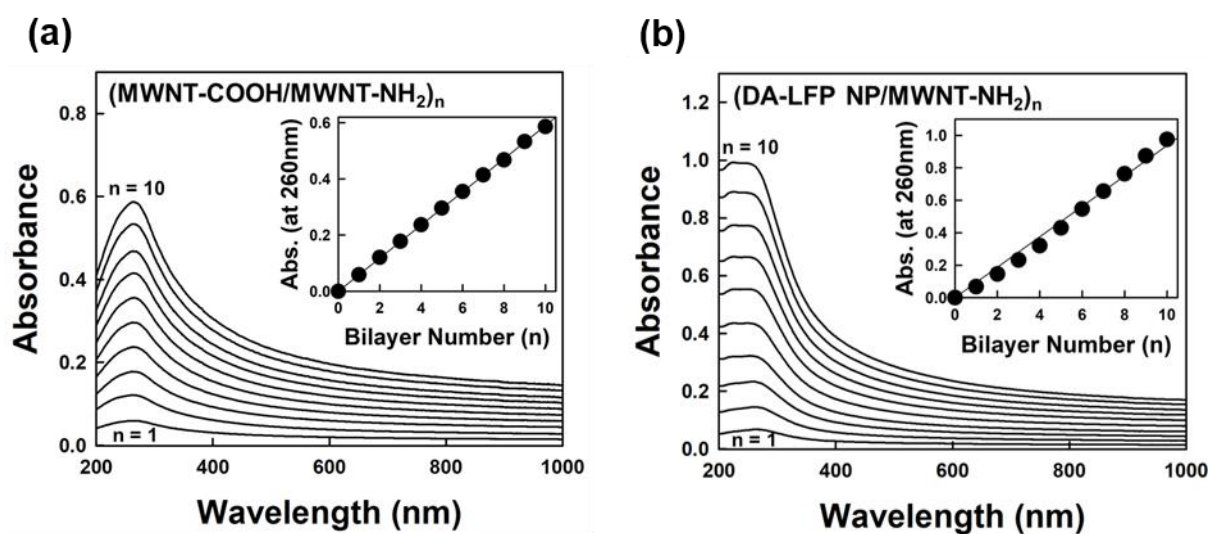
Figure S6. UV‑vis absorption spectra of (a) (MWNT‑COOH/MWNT‑NH$_2$)$_n$ and (b) (DA‑LFP NP/MWNT‑NH$_2$)$_n$ multilayers as a function of bilayer number (*n*). The insets indicate the absorption values at the wavelength of 260 nm according to difference bilayer number (*n*) of the multilayers, showing almost linear growth.
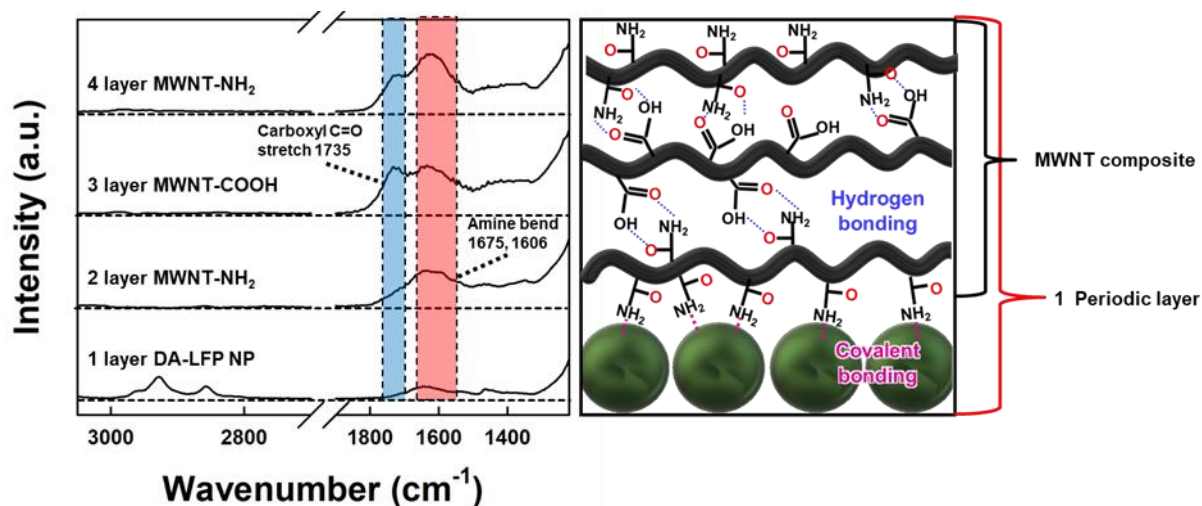
Figure S7. FTIR spectra of the (DA-LFP NP/MWNT-composite)$_{m=1}$ multilayer film as a function of the layer number. Here, the MWNT-composite refers to MWNT-NH$_2$/MWNT-COOH/MWNT-NH$_2$ multilayer composite. With deposition of MWNT-NH$_2$ layer onto the DA-LFP NP-coated substrate (1 layer), the C-H stretching vibration mode (at 2850−2950 cm^{-1}) caused by of DA ligand were noticeably disappeared, whereas the intensities of the N-H bending vibration mode originating from MWNT-NH$_2$ were increased. Additionally, the sequential deposition of MWNT-COOH (3 layer) and MWNT-NH$_2$ (4 layer) derives the increase of peak intensities from C=O (due to carboxyl group of MWNT-COOH) and N-H modes, however, there are no changes in C-H stretching modes.
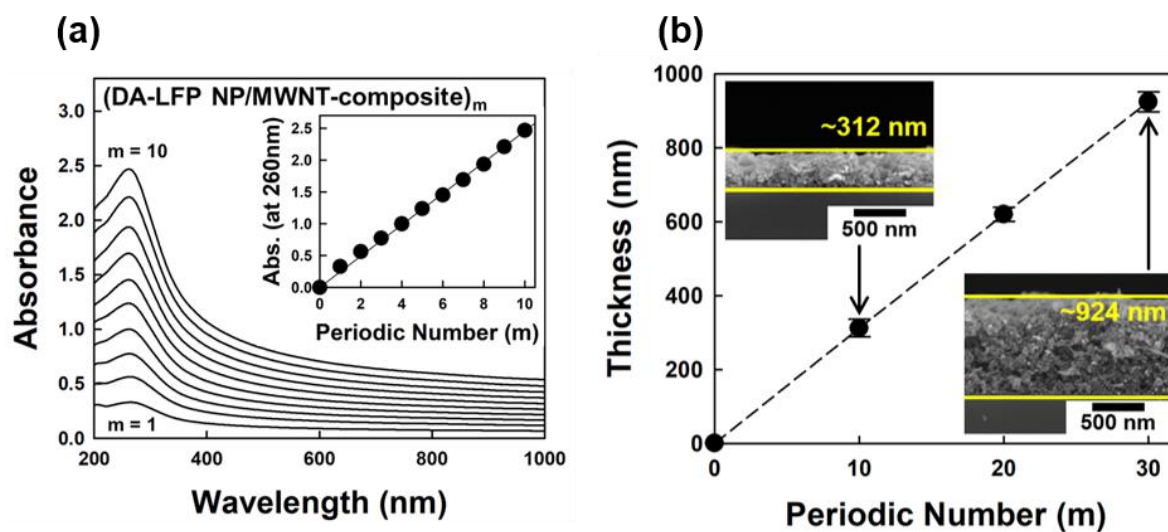
Figure S8. (a) UV-vis spectra of the (DA-LFP NP/MWNT-composite)$_m$ multilayers with difference periodic number (m). The inset indicates the absorbance of the multilayer films at wavelength of 260 nm, showing the regular growth with increasing periodic number (m). (b) Film thickness of the (DA-LFP NPs/MWNT-composite)$_m$ multilayers as a function of the periodic number (m) obtained from cross-sectional FE-SEM images. As the periodic number (m) increased from 10 to 30, the film thickness increased regularly from ~312 to ~924 nm.
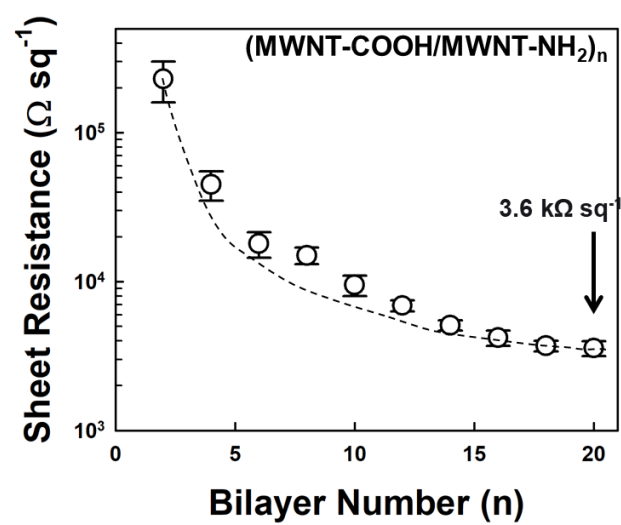
Figure S9. Sheet resistances of the (MWNT-COOH/MWNT-NH$_2$)$_n$-coated textiles as a function of the bilayer number (*n*).
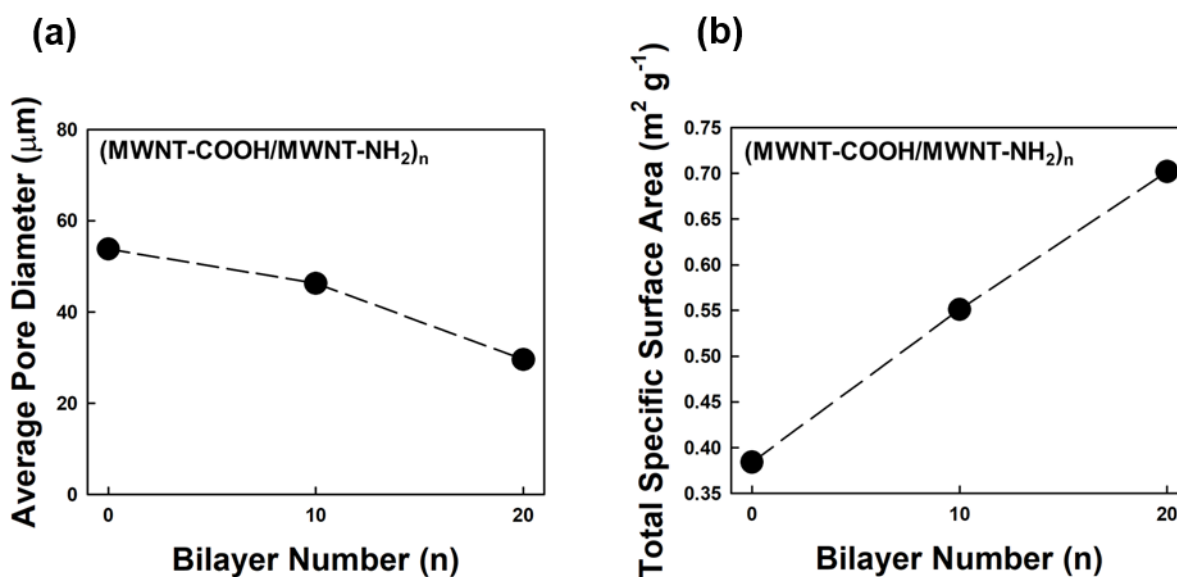
Figure S10. Bilayer number (n)-dependent (a) average pore diameter (µm) and (b) total specific surface area ($m^2 \, g^{-1}$) for the (MWNT-COOH/MWNT-NH$_2$)$_{n=10,20}$-coated textiles analyzed by mercury intrusion porosimetry (MIP). Here, the values at $n=0$ in each Figure is for the bare textile without MWNT coating. The average pore size of the textile electrode has gradually decreased form ~53.8 (for bare textile) to ~29.6 (for $n=20$) due to a number of newly introduced nanopores from the (MWNT-COOH/MWNT-NH$_2$)$_n$ multilayers coated on the textile surface (Figure S10a), while the specific surface area was increased (Figure S10b). In all measurements, the sample size is fixed at $3 \times 10 \, cm^2$.
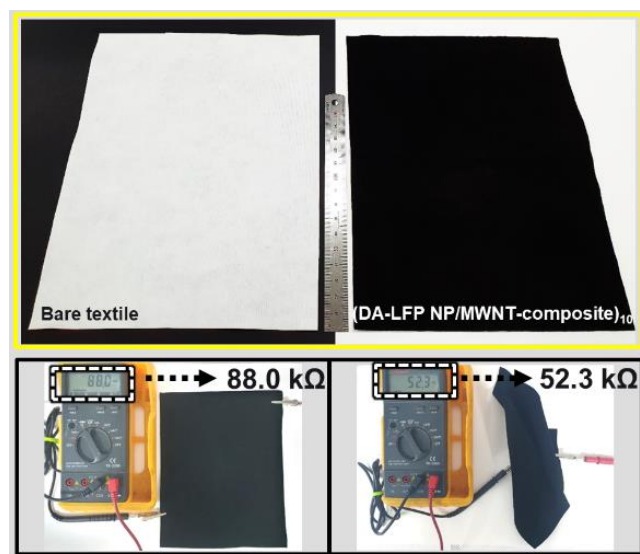
Figure S11. Photographs of the (DA-LFP NP/MWNT-compostie)$_{10}$-coated textiles with large area of 17×22 cm^2 (top). The ruler between the textile is 15-cm-scale. The (DA-LFP NP/MWNT-compostie)$_{10}$-coated textile maintained its electrical property even under severe mechanical deformation, indicating good film stability (bottom). The slight decrease in resistance after mechanical deformation may be due to the closely connected MWNT networks caused by the mechanical stress allowing facile electron percolation.
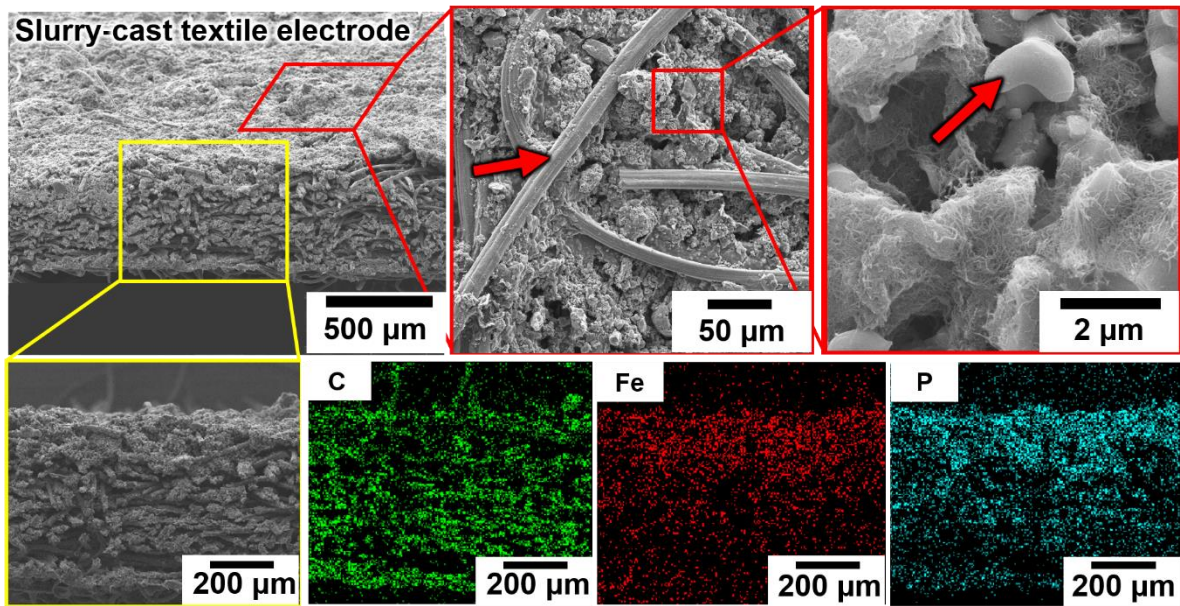
Figure S12. FE-SEM and EDS elemental mapping images of the textile electrode fabricated by conventional slurry casting method. In this case, the active slurry was prepared by physical mixing of commercially available LFP powder (average diameter of ~5 µm), functionalized MWNT (MWNT-COOH and MWNT-NH$_2$), and polymer binder (PVDF) with weigh ratio of 6.5:2.5:1. Although the EDS mapping images show that the casted slurry is well-penetrated into the textile, a poor interaction between each electrode component causes the insufficient coating (see red arrow) on textile fiber and NP surface, resulting in significant loss of energy and rate efficiency in electrochemical battery application.
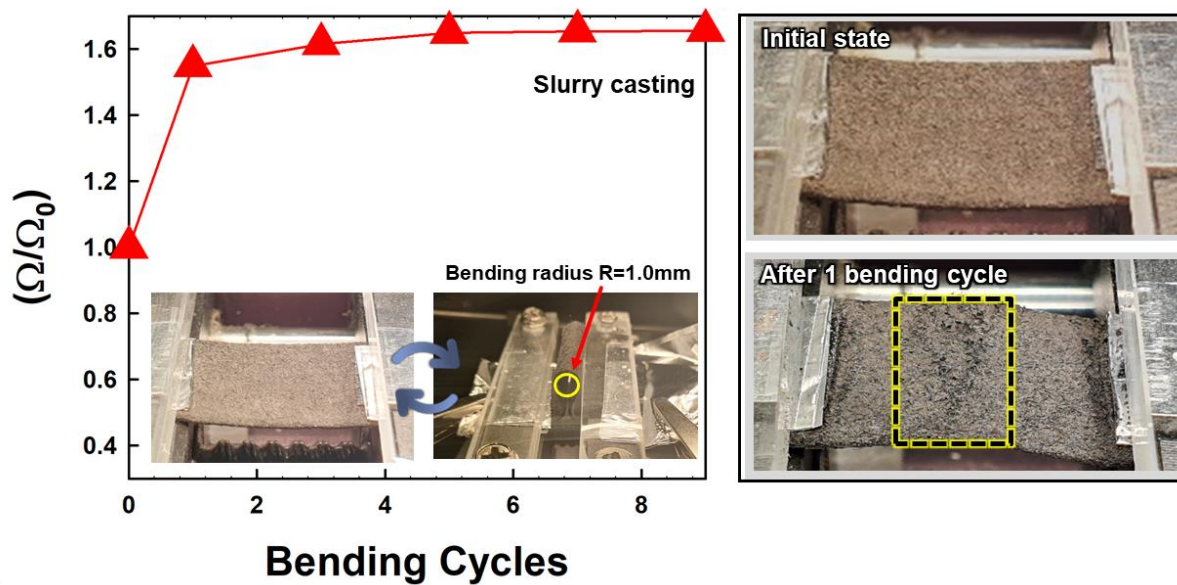
Figure S13. Resistance change (Ω/Ω_0) of the LFP/MWNT slurry-casted textile electrode with different bending cycles. In this case, the slurry-based textile electrode produced noticeable cracks and delamination of the active layer in only one bending (see dashed yellow box), resulting in a sharp increase in resistance.
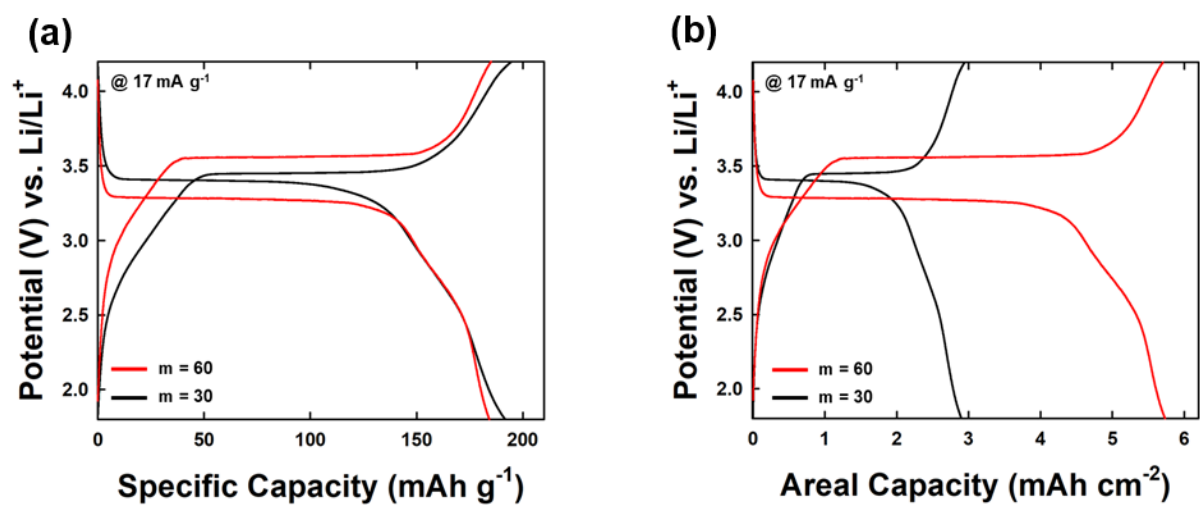
Figure S14. GCD curves of the (DA-LFP NP/MWNT-composite)$_{m=30 \text{ and } 60}$-coated textile electrodes at a current density of 17 mA g^{-1} for (a) areal capacity and (b) specific capacity.
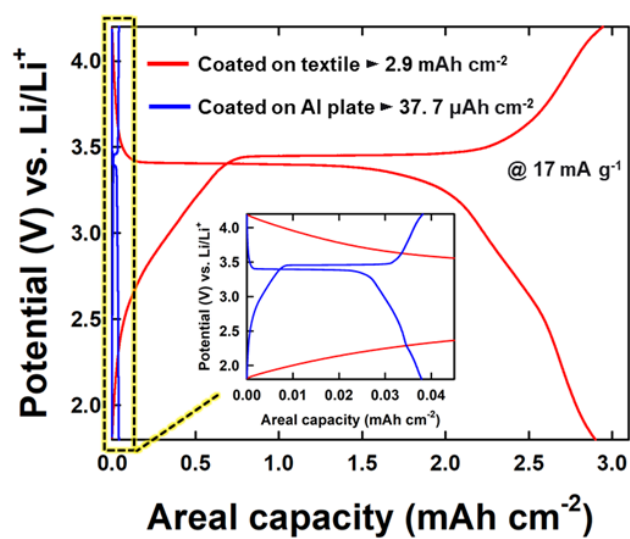
Figure S15. GCD profiles of the (DA-LPF NPs/MWNT-composite)$_{30}$-based electrodes prepared using textile (red solid line) and Al plate (blue solid line). In this case, the textile-based electrode showed ~77 times higher areal capacity (2.9 mAh cm^{-2}) than Al plate-based electrode (37.7 µAh cm^{-2}).
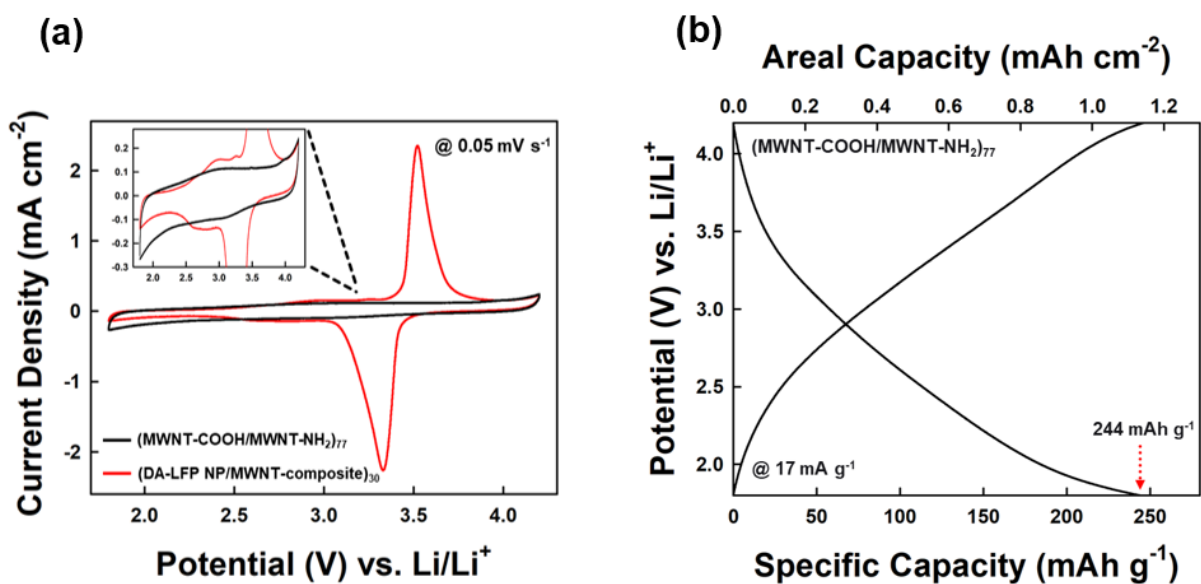
Figure S16. (a) Cyclic voltammograms of (MWNT-COOH/MWNT-NH$_2$)$_{77}$- and (DA-LFP NP/MWNT-composite)$_{30}$-based textile electrodes in potential window of 4.2 – 1.8 V (vs. Li/Li$^+$). Inset indicates an enlarged CVs in ± 0.3 mA cm^{-2}. In this case, the bilayer number of MWNT-COOH/MWNT-NH$_2$ multilayers was adjusted to 77 in order to equalize the amount of MWNTs in each electrode. (b) GCD profile of the (MWNT-COOH/MWNT-NH$_2$)$_{77}$-coated textile electrode performed at a current density of 17 mA g^{-1}.
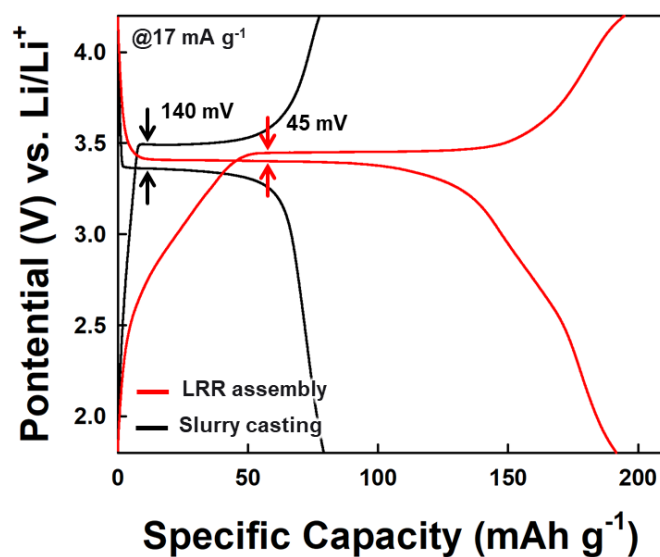
Figure S17. GCD profiles of the textile electrodes with difference preparation approaches (i.e., LRR assembly and conventional slurry casting). The specific capacities of each electrode show 191 mAh g^{-1} for LRR assembly (i.e., m=30) and 79.1 mAh g^{-1} for slurry casting, respectively. Additionally, the slurry-cast electrode exhibited about 3.1 times larger potential interval (140 mV) (the spacing between charge/discharge plateaus) compared to the LRR-assembled electrodes (45 mV), indicative of higher internal resistance.
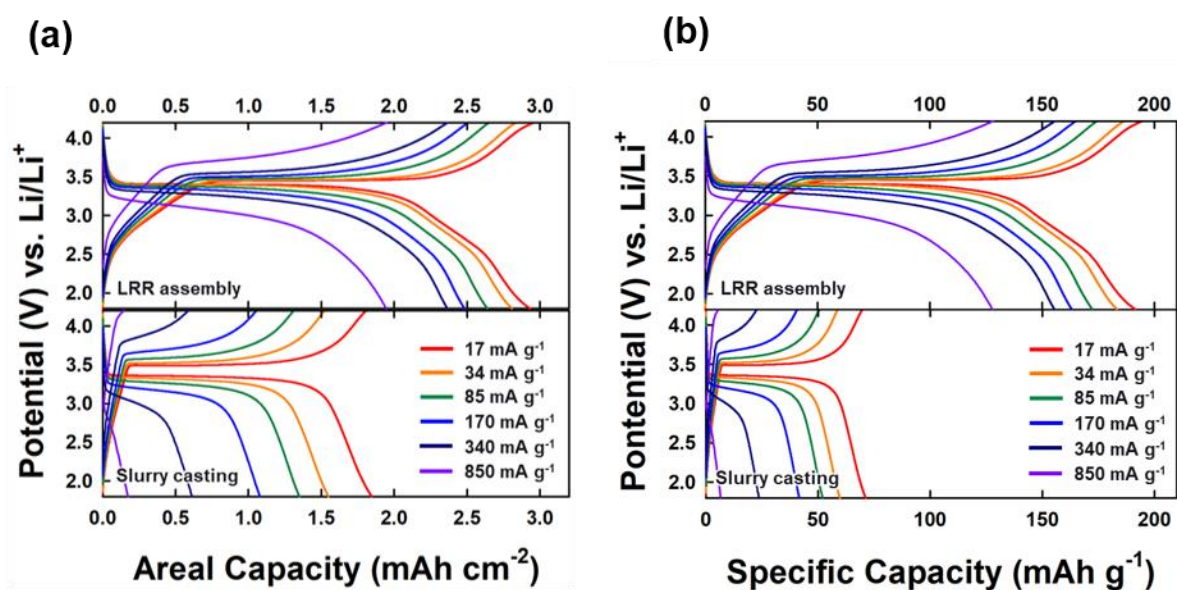
Figure S18. Comparison of (a) areal and (b) specific capacities for the textile electrodes prepared by LRR assembly (top) and conventional slurry casting method (bottom) measured by GCD test at various current densities ranging from 17 to 850 mA g^{-1}. In the case of the slurry casting-based electrodes, the GCD profiles at a current density of 850 mA g^{-1} showed nearly sloped line without noticeable voltage plateau, indicating a pseudocapacitive behavior that delivers a relatively lower capacity than for the Faradaic reaction.
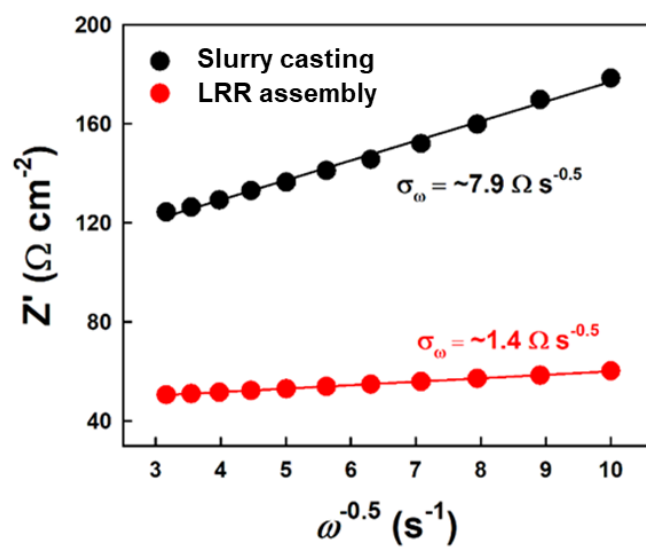
Figure S19. Relationship between resistance (Z′) and frequency ($\omega^{-0.5}$) in Warburg region for the LRR-assembled textile electrodes and the slurry-cast textile electrodes. The slop of each plot represents Warburg impedance coefficient (σ_ω).
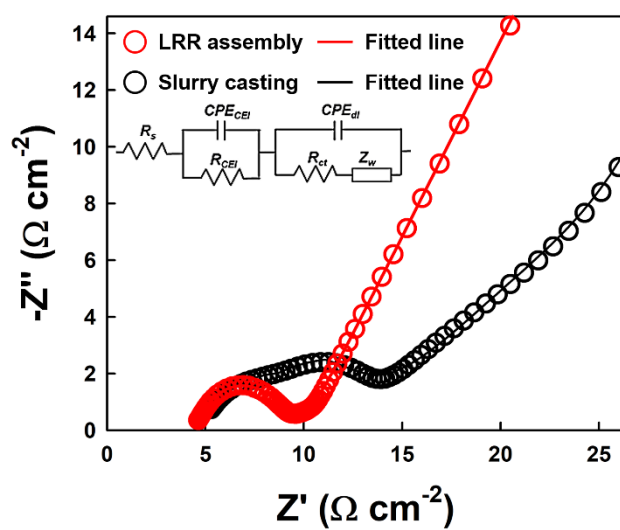
Figure S20. Nyquist plots for the textile cathode electrodes prepared by LRR assembly and slurry casting after 50th GCD cycle. The inset indicates representative equivalent circuit of the electrodes.
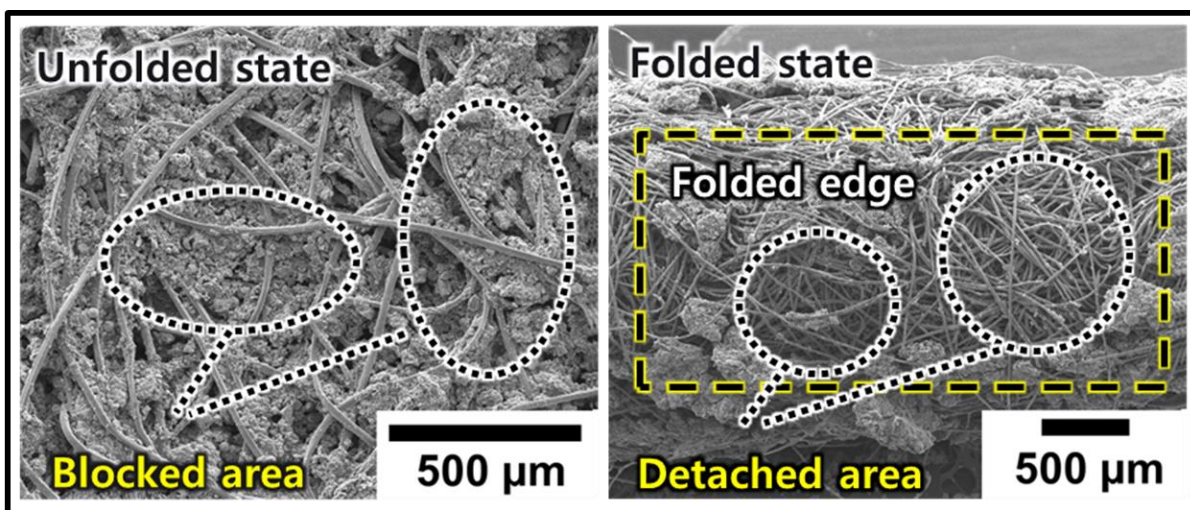
Figure S21. SEM images of slurry-cast textile electrodes with areal mass density of 23.3 mg cm^{-2} before and after folding. In this case, the partially aggregated slurry composites that was clogging the pores of the textile substrates showed noticeable delamination from the MWNT networks after fully folding.
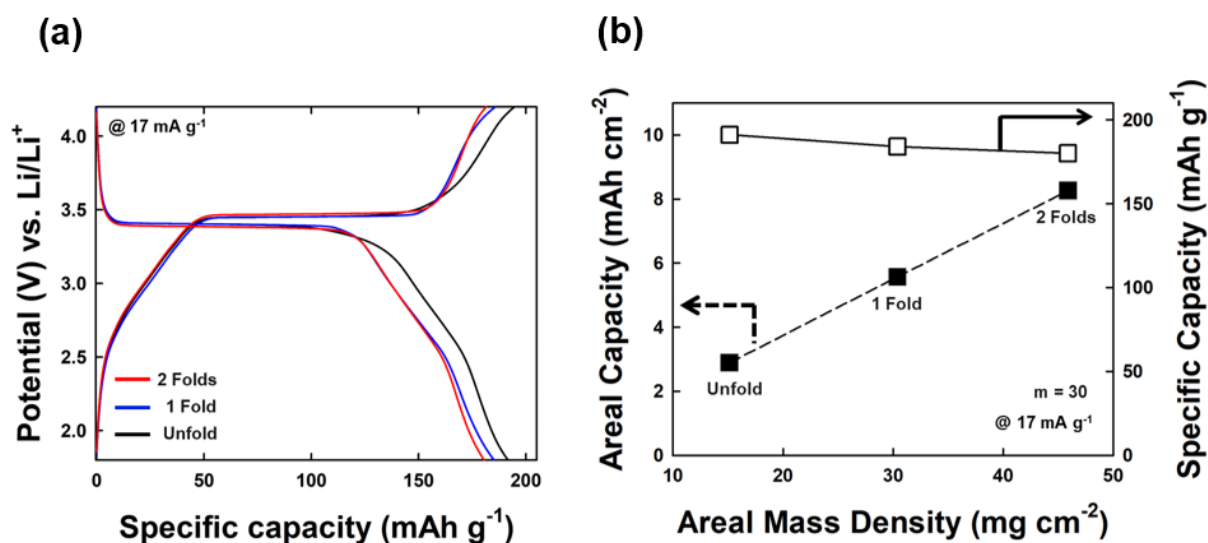
Figure S22. (a) GCD profiles of LRR-assembled textile electrodes (i.e., (DA-LFP NP/MWNT-composite)$_{m=30}$) with different folding number. Each folding number is corresponding to areal mass density of 15.2 (unfold), 30.4 (1 fold), and 45.9 (2 folds), respectively. (b) Change in areal and specific capacities for LRR-assembled textile electrodes at different areal mass densities (i.e., folding numbers). In this case, the specific capacity of the LRR-assembled textile electrode was measured to be 191.0, 184.5, and 180.2 mAh g^{-1} at a folding number of 0, 1, and 2. In all cases, the electrode area is 1×1 cm^2.
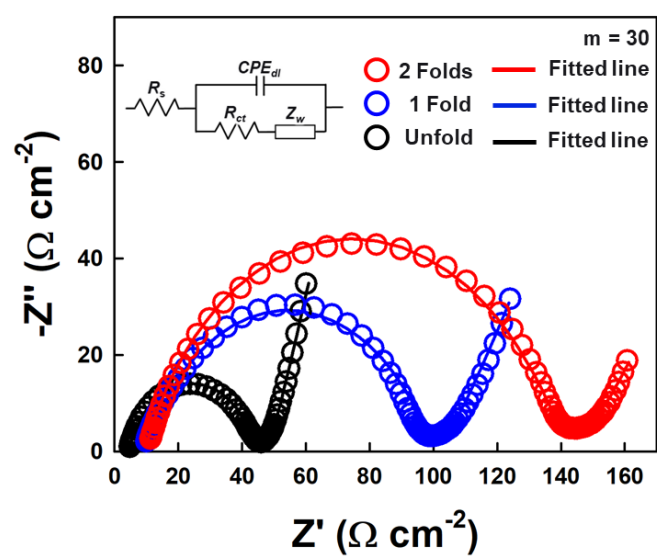
Figure S23. Nyquist plots of (DA-LFP NP/MWNT-composite)$_{30}$-coated textile electrodes with different folding number (0, 1, and 2). Inset shows representative equivalent circuit of obtained impedance spectra.
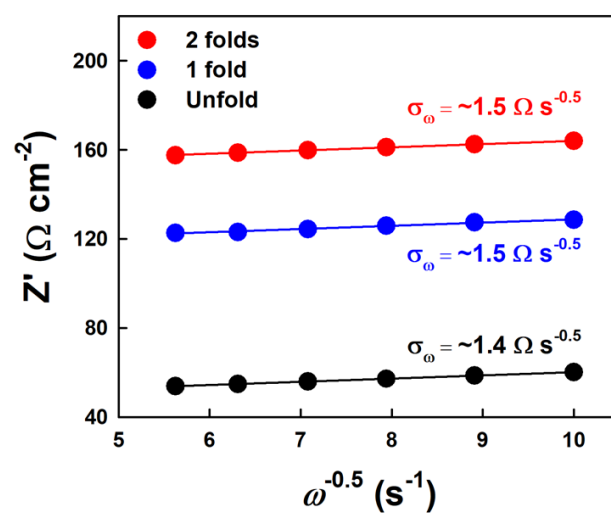
Figure S24. Plots of Z′ (Ω cm^{-2}) versus $\square^{-0.5}$ (s^{-1}) for the LRR-assembled textile electrodes with different folding number. In this case, the Warburg impedance coefficient ($\sigma_\square$) of each electrode was calculated from the Nyquist plot in **Figure S23**.

Table S1. Performance comparison of LFP or LCO-based textile-type LIB cathode electrodes. In this case, each capacity was summarized based on the highest value provided in each literature.

Electrode material (substrate)	Electrode preparation method	Mass density (mg cm^{-2})	Areal capacity (mAh cm^{-2})	Specific capacity (mAh g^{-1})	Ref.¶
(LFP NP/MWNT-composite)$_m$ (cotton textile)	LRR assembly*	15.2	2.9 @ 0.1C (m=30)	196 @ 0.1C (m=10)	**Our work**
2-folded (LFP NP/MWNT-composite)$_{30}$ (cotton textile)	LRR assembly*	45.9	8.3 @ 0.1C	180.2 @ 0.1C	**Our work**
LFP/Cellulose nanofiber/Carbon black/PVDF (Cellulose nanopaper)	Slurry casting	20	3.2 @ 0.1C	161 @ 0.1C	[S7]
LFP/rGO/PTFE (carbon fabric)	Slurry casting	8	1.20 @ 0.25C**	149 @ 0.25C	[S8]
LFP/Cellulose/Graphite (Filter paper)	Slurry casting	8	1.2 @ 0.1C**	146 @ 0.1C	[S9]
LFP/PDDA/PSS (carbon cloth)	Electrostatic self-assembly	5.2	0.82 @ 0.1C**	158 @ 0.1C	[S10]
LFP (carbon paper)	Impregnation-carbothermal reduction	2.8	0.22 @ 0.2C	79.3 @ 0.2C**	[S11]
LCO/Carbon black/PVDF/CNT (Nonwoven fibrous membrane)	Slurry casting	12.5	1.7 @ 0.13C**	134 @ 0.13C	[S12]

LCO/CNT/Cellulose (Filter paper)	Slurry casting	8.2	1.2 @ 0.2C**	140 @ 0.2C**	[S13]
LCO/PVDF (Carbon cloth)	Slurry casting	2	0.22 @ 0.7C	107 @ 0.7C	[S14]
LCO (Carbon cloth)	Hydrothermal reduction	1.4	0.17 @ 0.5C	130 @ 0.5C	[S15]

* LRR assembly: ligand replacement reaction-mediated layer-by-layer assembly.

** Calculated from given data in the literature.

Supporting References

[S1] Y.-H. Rho, L. F. Nazar, L. Perry, D. Ryan, *J. Electrochem. Soc.* **2007**, *154*, A283.

[S2] R. Dedryvère, M. Maccario, L. Croguennec, F. L. Cras, C. Delmas, D. Gonbeau, *Chem. Mater.* **2008**, *20*, 7164.

[S3] N. N. Sinha, C. Shivakumara, N. Munichandraiah, *ACS Appl. Mater. Interfaces* **2010**, *2*, 2031.

[S4] J. Tu, K. Wu, H. Tang, H. Zhou, S. Jiao, *J. Mater. Chem. A* **2017**, *5*, 17021.

[S5] K. Zaghib, A. Mauger, F. Gendron, C. M. Julien, *Chem. Mater.* **2008**, *20*, 462.

[S6] G. Vuković, A. Marinković, M. Obradović, V. Radmilović, M. Cˇolić, R. Aleksić, P. S. Uskoković, *Appl. Surf. Sci.* **2009**, *255*, 8067.

[S7] Y. Kuang, C. Chen, G. Pastel, Y. Li, J. Song, R. Mi, W. Kong, B. Liu, Y. Jiang, K. Yang, L. Hu, *Adv. Energy Mater.* **2018**, *8*, 1802398.

[S8] S. H. Ha, K. H. Shin, H. W. Park, Y. J. Lee, *Small* **2018**, *14*, 1703418.

[S9] S. Leijonmarck, A. Cornell, G. Lindbergh, L. Wagberg, *J. Mater. Chem. A* **2013**, *1*, 4671.

[S10] G. Tian, F. Scheiba, L. Pfaffmann, A. Fiedler, V. S. K. Chakravadhanula, G. Balachandran, Z. Zhao, H. Ehrenberg, *Electrochim. Acta* **2018**, *283*, 1375.

[S11] K. Kretschmer, B. Sun, X. Xie, S. Chen, G. Wang, *Green Chem.* **2016**, *18*, 2691.

[S12] A. M. Gaikwad, B. V. Khau, G. Davies, B. Hertzberg, D. A. Steingart, A. C. Arias, *Adv. Energy Mater.* **2015**, *5*, 1401389.

[S13] J. H. Han, K. H. Shin, Y. J. Lee, *ACS Appl. Mater. Interfaces* **2021**, *13*, 6375.

[S14] M.-S. Balogun, W. Qiu, F. Lyu, Y. Luo, H. Meng, J. Li, W. Mai, L. Mai, Y. Tong, *Nano Energy* **2016**, *26*, 446.

[S15] Q. Xia, M. Ni, M. Chen, H. Xia, *J. Mater. Chem. A* **2019**, *7*, 6187.